



ORIGINAL ARTICLE

Rapid microwave fabrication of new nanocomposites based on Tb-Co-O nanostructures and their application as photocatalysts under UV/Visible light for removal of organic pollutants in water



Pourya Mehdizadeh ^a, Mina Jamdar ^a, Makarim A. Mahdi ^b, Waleed K. Abdulsahib ^c, Layth S. Jasim ^d, Seyede Raheleh Yousefi ^a, Masoud Salavati-Niasari ^{a,*}

^a Institute of Nano Science and Nano Technology, University of Kashan, Kashan, P. O. Box. 87317-51167, Iran

^b Department of Chemistry, College of Education, University of Al-Qadisiyah, Diwaniya, Iraq

^c Department of Pharmacology and Toxicology, College of Pharmacy, Al-Farahidi University, Baghdad, Iraq

^d Department of Chemistry, College of Education, University of Al-Qadisiyah, Diwaniya, Iraq

Received 8 June 2022; accepted 10 January 2023

Available online 16 January 2023

KEYWORDS

TbCoO₃/TbO_{1.81} Nanocomposites;
Microwave Synthesis;
Photodegradation;
Hazardous pollutant;
Nano-photocatalyst;
Nanostructures

Abstract Herein, a novel and stable Tb-Co-O nanocomposite photocatalyst is fabricated through a one-pot microwave route for 2 min (600 W, 20 s On, 60 s Off), which is introduced as UV/Visible light active catalysts in wastewater treatment. Employing various combined parameters of Tb:Co ratio, pH adjustment agents, chemical and natural templates, the resulting nanostructures displayed the intrinsic structure nature, narrow size distribution, good optical properties, and excellent photocatalytic efficiency. The formation of Tb-Co-O nanostructures and their features were verified *via* X-ray diffraction (XRD), Fourier transform infrared spectroscopy (FT-IR), field-emission scanning electron microscopy (FE-SEM), transmission electron microscopy (TEM), and ultraviolet–visible diffuse reflection spectroscopy (DRS) technologies. Detailed physic-chemical measurements exhibited that all as-prepared nano-photocatalysts possesses both cubic (TbO_{1.81}) and orthorhombic

* Corresponding author.

E-mail address: salavati@kashanu.ac.ir (M. Salavati-Niasari).

Peer review under responsibility of King Saud University.



Production and hosting by Elsevier

(TbCoO₃) crystal structures. Furthermore, optical characterization by DRS developed light-sensitive channelization with band-gap energies at approximately 2.95 and 3.20 eV for Tb-Co-O nanocomposites. Finally, the photocatalytic studies of the resulting nanocomposites were compared by determining the elimination of Erythrosine (EY), Acid Violet 7 (AV7), and Acid Black 1 (AB1) under UV and Visible light illumination. As a result, the TbCoO₃/TbO_{1.81} nanocomposites with molar ratio of 1:3 (Tb:Co), valerian distillate as natural directing agent and ethylenediamine (en) as alkaline template yielded the optimum degradation percentage of 88 % for EY dye under the reaction condition of 10 ppm dye concentration in the presence UV light toward other pathways. Also, we proposed a mechanistic insight of photodegradation based on the radical scavengers, which revealed that h⁺ did the important role, and OH• and •O₂⁻ represented an irrelevant role in the degradation of EY. The current study offers an effective way for development of a high-efficiency Tb-Co-O photocatalyst in eliminating dyes from contaminant water.

© 2023 The Author(s). Published by Elsevier B.V. on behalf of King Saud University. This is an open access article under the CC BY-NC-ND license (<http://creativecommons.org/licenses/by-nc-nd/4.0/>).

1. Introduction

The quality of the surface water has a significant impact on the ecosystem and a variety of energetic and environmental issues. With increasing human population and industrial advances, concerns for environmental protection, waste management, pollution control, and safe supply of drinking water have been increased. In developing countries as well as industrialized countries, the amount of pollution entering the water as a result of human activities is constantly increasing (Lee and Park, 2013; Zhang et al., 2013; Yahya et al., 2018). Dyes are one of the most dangerous water-soluble pollutants that their removal from aquatic environments has received much attention due to their toxicity, high durability and degradation-resistant (Jusoh et al., 2013). For example, Erythrosine (EY) as a water-soluble xanthene dye is widely used in drugs, cosmetics and food productions. However, it is well known that high level of this dye can exert various types of thyroid activities, allergies, DNA damage behavior, carcinogenic in nature (Mittal et al., 2006; Kaur and Gupta, 2012). Notably, a number of studies have also been reported on the decomposition of Azo dyes, namely, Acid Violet 7 (AV7) and Acid Black 1 (AB1), which are most difficult to degrade. These compounds with -N=N- bonds in association with complex aromatic structures and sulfonic acid groups are regarded as the highly recalcitrant and genotoxic types in comparison with other azo dyes (Paprocki et al., 2010; González-Casamachin et al., 2019). Textiles, dyeing and printing industries are one of the largest consumers of water and consequently are the main producers of dye contaminants in wastewater (Malathi and Madhavan, 2017; Malathi et al., 2018). The discharge of untreated industrial effluents into aqueous environments has worsened the situation of water resources around the world. Advanced oxidation processes (AOPs) have been discovered as the most effective method for the removal of resistant organic pollutants (Miranda-García et al., 2010). The main characteristics of AOPs are in produced oxidant species like hydroxyl radicals. Hydroxyl radicals with unique advantages like high oxidation power and a potential of 2.8 V have a significant responsibility in the destruction of organic compounds (Wang and Xu, 2012). In AOPs, different methods are involved to form highly potential active oxidants. Given these aims, four general categories such as (i) primary oxidants (hydrogen peroxide (H₂O₂), ozone (O₃)), (ii) energy sources (UV light, heat and ultrasonic waves), (iii) catalysts and (iv) Fenton's reagent have been proposed (Leong et al., 2014; Ong et al., 2018). Meanwhile, photocatalytic oxidation technology as an environmentally friendly route can oxidize diverse organic pollutants such as dyes and antibiotics into inorganic ions without causing secondary pollution. Following this discovery, a series of metal oxide semiconductors (e.g., ZnO (Singhal et al., 2022), TiO₂ (Nur et al., 2022), CdO (Saravanakumar et al., 2018), MnO₂ (Chiam et al., 2020), Fe₂O₃ (Zhang et al., 2010) and etc.) have been applied to address the demands of photo-

degradation process. However, since 1972, TiO₂ semiconductors have been considered to be the most popular photocatalysts because of their high stability, low cost, and non-toxic properties (Fujishima and Honda, 1972; Upadhyay et al., 2014). But, the wide energy gap (E_g ~ 3.2 eV) of TiO₂ nanostructures limits their performance in the visible region and increases a positive effect in the near UV region (about 5 % of the total solar radiation) (Meng et al., 2019; Xu et al., 2019). To address these drawbacks, significant efforts have been performed on the development of the nano-photocatalysts with narrow band gaps, for example; ZnIn₂S₄ (He et al., 2019; Wang et al., 2019), g-C₃N₄ (Wen et al., 2017; Teng et al., 2019; Xia et al., 2020), Fe₂O₃/EuVO₄/g-C₃N₄ (Monsef et al., 2021a), PrVO₄/CdO (Monsef et al., 2021b), and LaCoO₃ (Wang et al., 2015). Among recent researches, perovskite-type structures formulated by LnCoO₃ (Ln = La-Y, RE) are introduced as a superior semiconductor for advance photocatalytic activity (Jung and Hong, 2013; Wang et al., 2015; Guo et al., 2019; Michel et al., 2019; Salavati-Niasari, 2006). In fact, these ceramic systems with the involvement of both the 3d- and 4f-cations exhibit considerable properties like magneto-electronic phase separation (Wang et al., 2016; Gavrikov et al., 2020). Based on these properties, the applicability of Ln cobaltite in diverse fields such as solid state oxide fuel cells (SOFCs) (Enrico and Costamagna, 2014), thermoelectric (Moon et al., 2000; Jiamprasertboon et al., 2014), gas sensors (Mochinaga and Arakawa, 2001), oxidation of CO (Álvarez-Galván et al., 2011), and photocatalysis (Wang et al., 2020; Salavati-Niasari, 2009) gains remarkable attention. However, TbCoO₃ as a member of the rare-earth perovskites in different photocatalysis directions has recently received less attention. The preparation way of perovskite structures plays a vital role in yielding quality of the final products in terms of dimension size and structural stability. Microwave heating route has the advantages of spontaneous reaction time, cleaner environment and lower manufacturing costs (Gerbec et al., 2005) compared to other wet chemical methods such as hydrothermal (Megarajan et al., 2015), combustion (Tugova and Karpov, 2021) and sol-gel pechini routes (Wu et al., 2018). However, the controlled morphology of nano-products can be realized in template materials and correlation of green nanoreactors for the crystal growth and nucleation process. To date, the chemical and natural precursors have been adopted as surface-active stabilizers for the fabrication of nano-sized mesoporous material. Template materials have a pivotal role in reducing the condensation reaction and preventing particle agglomeration. In this study, novel nanocomposites based on Tb-Co-O (TbCoO₃/TbO_{1.81}) nanostructures is fabricated through a one-pot microwave route, which is introduced as UV/Visible light active catalysts in wastewater treatment. Also, various combined parameters of Tb:Co ratio, pH adjustment agents, chemical and natural templates were employed to evaluate the structural, morphological and optical properties. This configuration of the perovskite-type based on

Tb-Co-O illustrated a comparison study of photodegradation efficiency under UV and visible light illumination by investigating Erythrosine (EY), Acid Violet 7 (AV7), and Acid Black 1(AB1) as pollutant models.

2. Experimental

2.1. Materials and characterization equipment

The starting chemicals used in preparing the samples, including terbium nitrate hexahydrate ($\text{Tb}(\text{NO}_3)_3 \cdot 6\text{H}_2\text{O}$), cobalt(II) acetate tetrahydrate ($\text{Co}(\text{CH}_3\text{CO}_2)_2 \cdot 4\text{H}_2\text{O}$), polyvinylpyrrolidone (PVP), and tetraethylenepentamine (TEPA) were procured from Sigma-Aldrich Company. Also, ethylene glycol (EG), poly vinyl alcohol (PVA), ethylenediamine (en), and ammonia (NH_3) were obtained from Merck and utilized as received without further purification. Crystalline phase of the nanostructured composites were recorded by a Philips-X'pertpro, X-ray diffraction was performed using Ni-filtered $\text{Cu K}\alpha$ radiation. Scanning electron microscopy (SEM) images were obtained on an LEO-1455VP system equipped with energy-dispersive X-ray spectroscopy. EDX analysis with 20 kV accelerated voltage was administered. Fourier-transform infrared (FT-IR) spectra were recorded on a Nicolet Magna-550 spectrometer using KBr pellets. Transmission electron microscopy (TEM) images were obtained on a Philips EM208 transmission electron microscope with an accelerating voltage of 200 kV. The N_2 adsorption/desorption analysis (BET) was performed at -196°C using an automated gas adsorption analyzer (Tristar 3000, Micromeritics). The pore-size distribution was calculated by using the desorption branch of the isotherm according to the Barrett, Joyner, and Halenda (BJH) method. The light absorbance attribute of the Tb-Co-O nanostructures was investigated with a UV-vis spectrophotometer (Shimadzu, UV-2550, Japan). Magnetic properties were measured using a vibrating sample magnetometer 60 (VSM, Meghnatis Kavir Kashan Co., Kashan, Iran).

2.2. Fabrication of Tb-Co-O nanocomposites

The magnetic $\text{TbCoO}_3/\text{TbO}_{1.81}$ nanostructures were synthesized *via* a facile microwave-assisted method. In the beginning, the stoichiometric amounts of terbium nitrate (0.54 g, 1.2 mmol) and cobalt acetate (1.0 g, 3.6 mmol) were separately dissolved in 40 mL of EG solvent and then well mixed under vigorous stirring. Then, 2 mL of valerian distillate as natural complexing agent was dropped into the mixture solution.

The suspension was stirred for 10 min and then treated with microwave radiation for 2 min (600 W, 20 s On, 60 s Off), while 1.25 mL of en as both precipitating and pH adjustment agent was dropwise blended to the above reaction. After that, the resulting products were centrifuged at 8000 rpm, washed frequently by H_2O and dried at 80°C . Finally, to remove

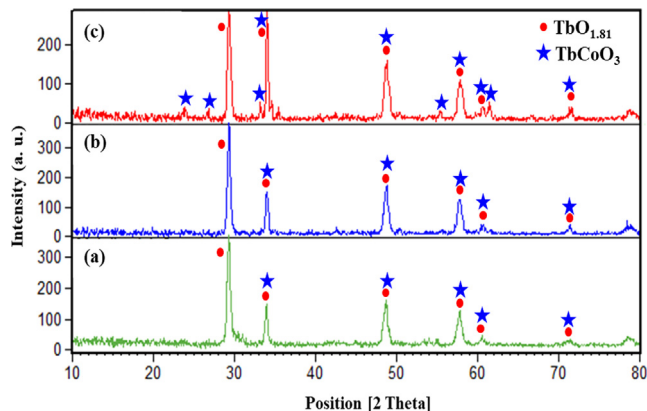


Fig. 1 XRD patterns of microwave synthesized Tb-Co-O nanocomposites in various molar ratios of Tb:Co (a-c) sample nos. 1-3.

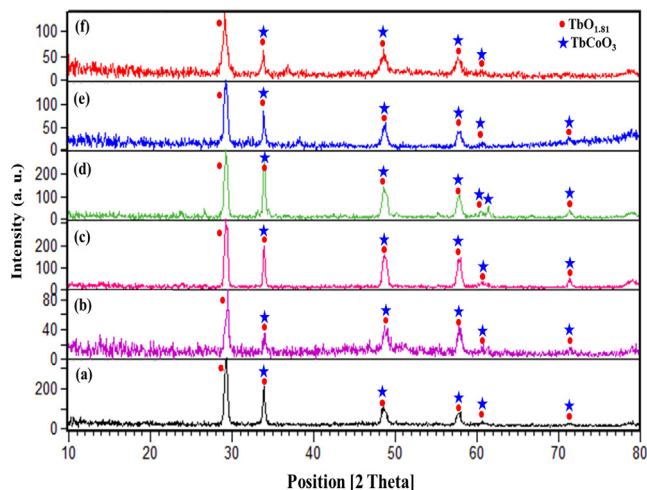


Fig. 2 XRD patterns of as-prepared Tb-Co-O nanocomposites synthesized at different conditions, namely, different directing templates and pH adjustment agents (a-f) sample nos. 4-9.

Table 1 Preparation conditions of Tb-Co-O nanocomposites.

Sample No	Tb:Co molar ratio	Type of capping agent		pH adjustment agent	$D_{\text{ave.}}/\text{XRD}$ (nm)
		Chemical	Natural		
1	1:1	–	–	en	19.58
2	1:3	–	–	en	22.74
3	1:5	–	–	en	27.24
4	1:3	PVA	–	en	19.41
5	1:3	PVP	–	en	23.05
6	1:3	–	Valerian	en	21.56
7	1:3	–	Orange blossom	en	22.03
8	1:3	–	Valerian	TEPA	21.26
9	1:3	–	Valerian	NH_3	20.38

any organic compound, the Tb-Co-O powders were calcined at 800 °C for 4 h. The impact of various combined parameters such as Tb:Co ratio, pH adjustment agents, chemical and natural templates on the structure nature and size distribution of the photocatalyst composites are illustrated in Table 1.

2.3. Photocatalytic experiments

The photocatalytic process of Tb-Co-O nanocomposites was conducted by decolorization of three different organic contaminants namely, EY, AV7, and ABI in a photoreactor (Pyrex glass) at room temperature. Typically, approximately 100 mg of catalyst powders was dispersed into 100 mL of pollutant

solution (with pH = 6.0, 10 ppm), while subjected to air bubbles, and continuous magnetic stirring. Before illumination tests, the suspension was treated in the dark medium for 0.5 h to assess the adsorption – desorption equilibrium between dye molecules and catalysts. At different time intervals of irradiation, 3 mL of the reaction solution was extracted to determine the concentration of organic pollutant using a UV–vis spectrophotometer. Experiments were checked under UV (Osram ULTRA-VITALUX 400 W) and visible lights (Osram 150 W) at approximately distance of 30 cm. To remove the catalyst particles, the samples were centrifuged at 15000 rpm for five minutes. The λ^{max} of 530 nm, 520 nm, and 495 nm were employed for measuring the concentration

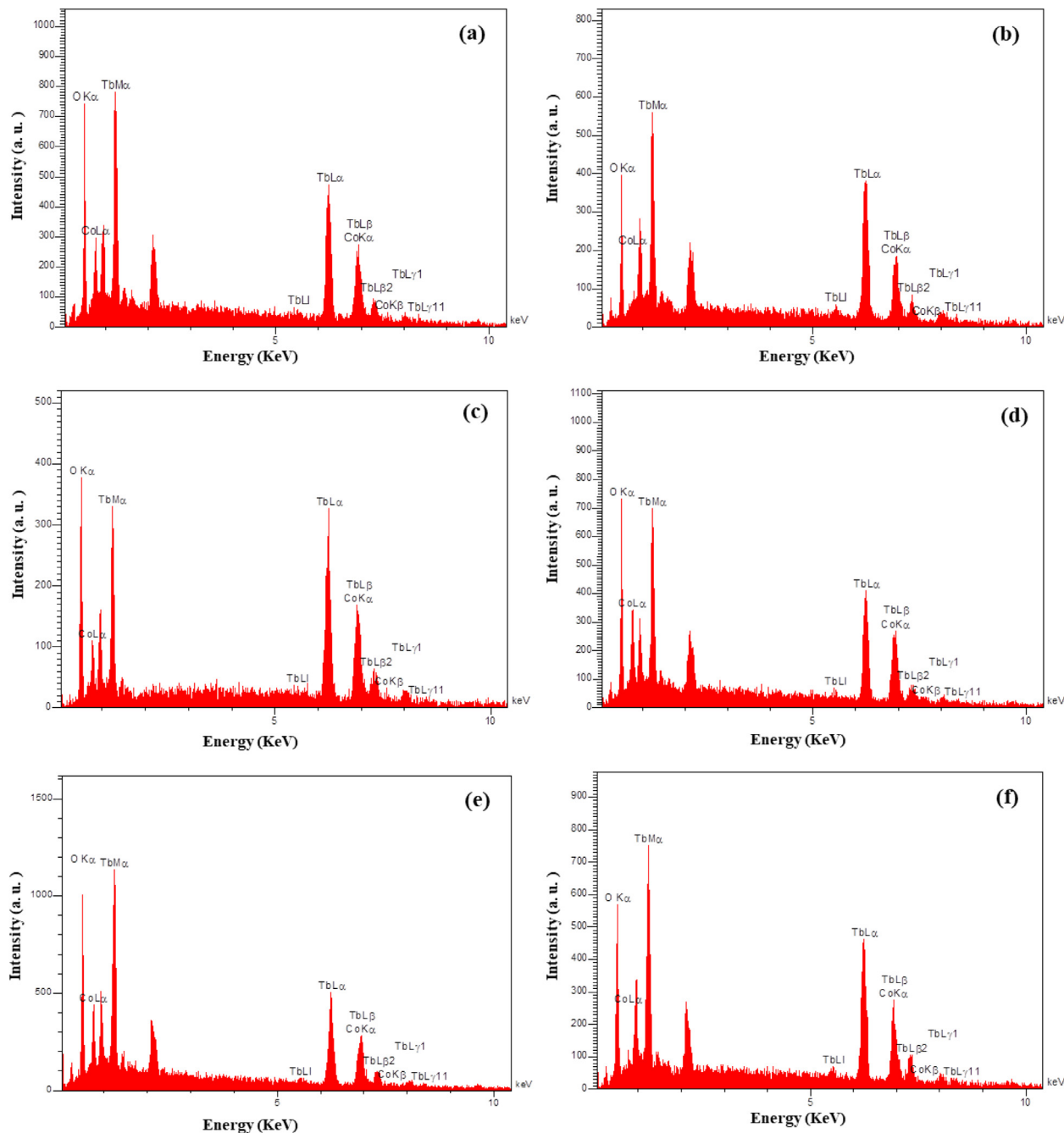


Fig. 3 EDS spectra of the sample nos. (a) 4, (b) 5, (c) 6, (d) 7, (e) 8, and (f) 9.

of EY, AV7, and AB1, respectively. The photodegradation efficiency (%) of nano-catalysts can be calculated using the following equation:

$$\%H = [(P_0 - P)/P_0] * 100 \quad (1)$$

Where H is the percentage of photo-degradation, P_0 is the initial absorbency of pollutant solution and P is the final absorbency of solution after UV-vis illumination.

3. Result and discussions

3.1. XRD patterns

The crystalline phase and composition nature of the products prepared under different operational circumstances were investigated *via* XRD measurements. Fig. 1 displays the effect of different Tb:Co molar ratios of 1:1 (sample no. 1), 1:3 (sample no. 2), and 1:5 (sample no. 3) on the purity and crystalline structure of the final products. As shown in Fig. 1, the XRD patterns follow the binary systems containing the $TbCoO_3$ (JCPDS No. 01-073-1196) and $TbO_{1.81}$ structures (JCPDS No. 01-075-0275). Notably, introduction of different metal ratios provide a variation in the relative peaks intensity along with clear crystalline phase. It should be noted that the sample no. 2 could potentially result in the strong crystallinity with the lowest crystallite size compared with other samples. It contains six diffraction peaks at 29.2° , 33.8° , 48.5° , 57.6° , 60.4° and 71.2° , corresponding to the diffraction planes (111), (200), (220), (311), (222), and (400) of cubic $TbO_{1.81}$ phase with the space group of $Fm-3m$, respectively. However, five overlapping peaks at 33.8° , 48.5° , 57.5° , 60.5° and 71.1° can be well indexed to the (112), (220), (311), (024) and (224) of orthorhombic $TbCoO_3$ phase with the space group of $Pbnm$, respectively, suggesting successful preparation of final products. Besides, additional peaks near 23.8° , 26.6° , 33.1° , 55.3° and 61.4° in sample no. 3 deliver the crystal formation of $TbCoO_3$ phase, which can be assigned to the (110), (111), (020), (114) and (312) faces, respectively. By changing the natural and chemical templates, the structural results in Fig. 2 show the same composition of orthorhombic $TbCoO_3$ (JCPDS No. 01-073-1196) and cubic $TbO_{1.81}$ (JCPDS No. 01-075-0275) structures. With considering the simple and massive bases, namely, NH_3 and TEPA, crystalline structure is

extremely matched with the composite patterns including $TbCoO_3$ and $TbO_{1.81}$ phases (Fig. 2(e, f)). The average crystallite sizes of the resulting nanocomposites were obtained from peak broadening of XRD pattern at its half maximum height in radians (FWHM) according to the Debye-Scherrer equation (Eq. (2)) (Monsef and Salavati-Niasari, 2021) and have been summarized in Table 1.

$$D : 0.9\lambda/\beta\cos\theta \quad (2)$$

Where D, λ , β , and θ are crystallite size of nano-sized samples, the X-ray wavelength of radiation (nm), FWHM, and diffraction angle, respectively.

3.2. EDS and FT-IR studies

The elemental composition of the resulting nanocomposites (sample nos. 4–9) was evaluated *via* EDS technique. Fig. 3(a-f) provides a signal observation of Tb, Co, and O elements for designed composites, describing formation of Tb-Co-O arrangements without any impurity. Furthermore, FT-IR analysis was used to examine the chemical groups and surface modifications of the $TbCoO_3/TbO_{1.81}$ nanocomposites. From Fig. 4, the FT-IR spectrum of Tb-Co-O nanostructures prepared with valerian as natural directing agent (sample no. 6) illustrate the appearance of two peaks at 3433 cm^{-1} and 1650 cm^{-1} , which may be attributed to the stretching and bending vibrational modes of O–H molecules, respectively (Salavati-Niasari et al., 2008). Also, some absorption peaks in the range of $400\text{--}850\text{ cm}^{-1}$ correspond to the overlapping vibrations for metal–oxygen and oxygen–metal–oxygen bands of perovskite Tb-Co-O nanocomposites, similar to other perovskite-type lanthanide cobaltite structures (Wang et al., 2020).

3.3. Morphology investigations

In this study, various chemical and natural surfactants as well as different types of alkaline agents were employed to examine the impact of active functional groups on particle size and shape of the final products. Fig. 5 displays the SEM images of the Tb-Co-O nanocomposites prepared with polymeric and natural templates. When polymeric templates (PVP and PVA) were used as surfactant, agglomerated structures were

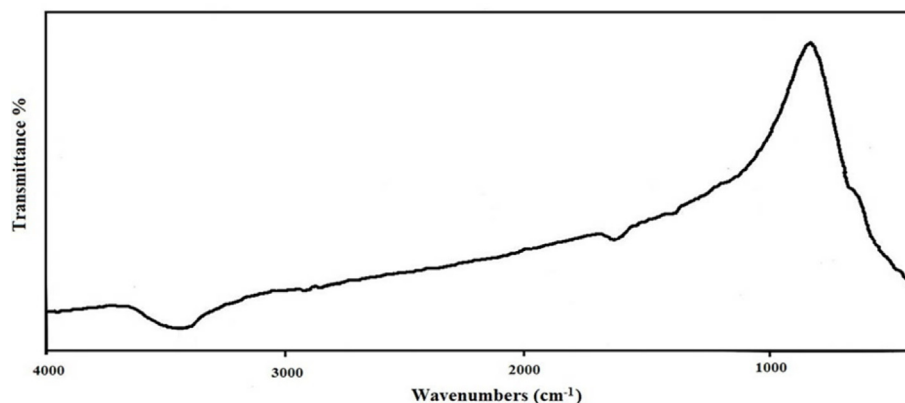


Fig. 4 FT-IR spectrum of sample no.6.

created. It can be seen that the templating environment of PVA show a dependent compact of particles in the range of 13.7–188.8 nm (sample no. 4). However, with considering PVP as soft polymeric template (sample no. 5), small irregular particles with diverse diameters from 13.6 to 155.6 nm were formed. But, by employing organic and natural templates like valerian extracts (sample no. 6), the uniformity arrangement of individual nanoparticles with mean nanosized diameter of 20.2 nm was organized, while another natural template like orange blossom extract offered microstructures consisting of non-uniform nanoparticles within the wide window from

13.5 to 125.5 nm (sample no. 7). The particle size histograms of the products (sample nos. 4, 5, 6, and 7) estimated from their FESEM images have been plotted in Fig. 5. As shown in this figure, sample no. 6 has a monodisperse diameter distribution of particles in the range of 10.4–32.0 nm. Therefore, the optimal template for in-situ synthesis of $\text{TbCoO}_3/\text{TbO}_{1.81}$ nanocomposites was valerian extracts. Valerian extract is one of the most widely consumed plants for medicinal purposes, which act as a collection of bioactive components such as alkaloids, isovaleramide, gamma aminobutyric acid, isovaleric acid, iridoids, sesquiterpenes, hydroxyvaleric acid and ace-

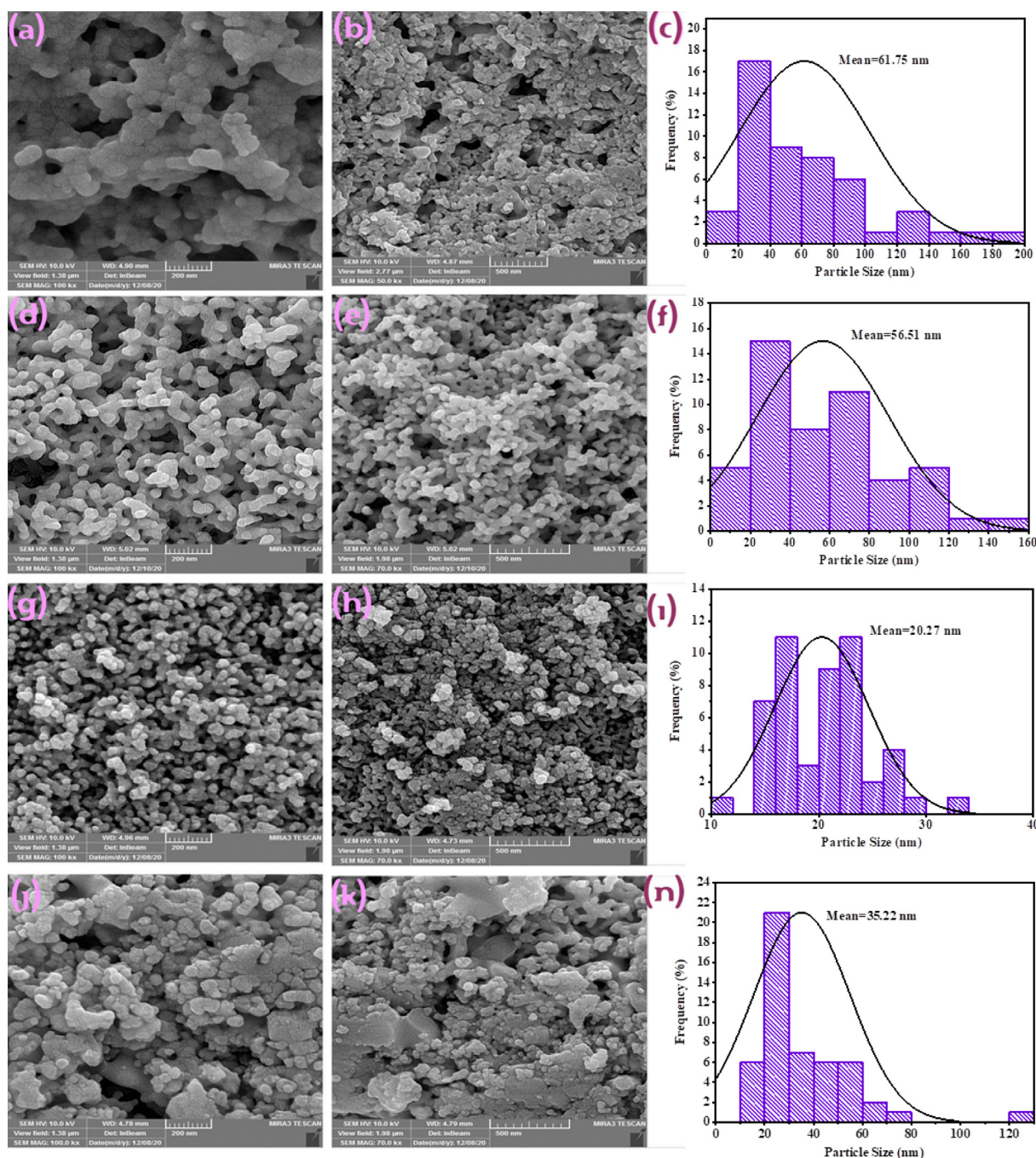


Fig. 5 The SEM images and corresponding particle size distribution of Tb-Co-O nanocomposites prepared with different chemical and natural surfactants (a-c) sample no.4, (d-f) sample no.5, (g-i) sample no.6, and (j-n) sample no.7.

toxyvaleric acid, flavanones and linarin (Yeganeh-Faal et al., 2017). In fact, this extract along with hydroxyl groups of amine template show a kinetic control over nucleation and growth of formed crystals, thus prevent nano-product agglomeration by creating spatial barrier around the metal cations. Fig. 6 shows the influence of simple (NH_3) and massive bases (TEPA) on the morphology and size distribution of Tb-Co-O nanocomposites. By considering NH_3 , en and TEPA as the alkaline agents, the SEM observation illustrates that en as pH adjustment agent can greatly produce the positive role on size of composite materials. When TEPA was applied to act as alkaline template, connected structure were created with wide ranging size of 19.9–161.7 nm (sample no. 8). Although, another simple alkaline agent (NH_3) resulted in the formation of agglomerated particles with particle size distribution of 14.7–138.8 nm (sample no. 9). TEM images were also used to examine exact details of morphological characteristics for samples produced in the presence of both valerian extracts and en as directing agents. Fig. 7 depicts the TEM images of optimized nanocomposites in two different scales (40 and 100 nm). Similarly to the SEM image, tiny nanoparticles with regular-shaped crystalline are formed.

3.4. BET analysis

In order to determine the surface characteristics of the Tb-Co-O nanocomposites prepared with valerian extract as natural chelating agent (sample no. 6), BET calculation was performed. Fig. 8 illustrates the nitrogen adsorption-desorption isotherms and corresponding pore size distribution plots of perovskite nanocomposites based on $\text{TbCoO}_3\text{-TbO}_{1.81}$ at

77 K. As a result, the obtained plots was organized in type IV isotherm with the hysteresis type H3, matching to IUPAC classification. The specific surface area, total pore volume and average pore size of the resulting nanocomposites in ideal circumstances was calculated to be $27.4 \text{ m}^2 \text{ g}^{-1}$, $6.29 \text{ cm}^3 \text{ g}^{-1}$ and 33.85 nm , respectively. These data provide new way for photocatalytic abilities of mesoporous materials in environmental cleaning.

3.5. Magnetic properties

The magnetic measurements of binary Tb-Co-O nanocomposites were further investigated within an applied field from $-15,000$ to $15,000 \text{ Oe}$. As shown in Fig. 9, the optimized samples possess the ferromagnetic nature by the hysteresis loop. The magnetic parameters of sample no.6 such as saturation magnetization (M_s), residual magnetization (M_r), and coercivity (H_c) values were 0.085 emu/g , 0.014 emu/g , and 150 Oe , respectively. High magnetic behavior of these binary nanocomposites offers their easy cycling performance during photo-degradation reaction tests.

3.6. UV – Vis DRS characterization

The DRS analysis was utilized to determine the photon receptive behavior for binary $\text{TbCoO}_3\text{/TbO}_{1.81}$ nanocomposites. Fig. 10 provides the initial information on the electronic structure and optical characteristics of Tb-Co-O photocatalysts. This data offer the typical absorption peaks at around 300–400 nm. The intensive absorption thresholds in the energy gap quantity of binary nanostructures are seen at nearly 386

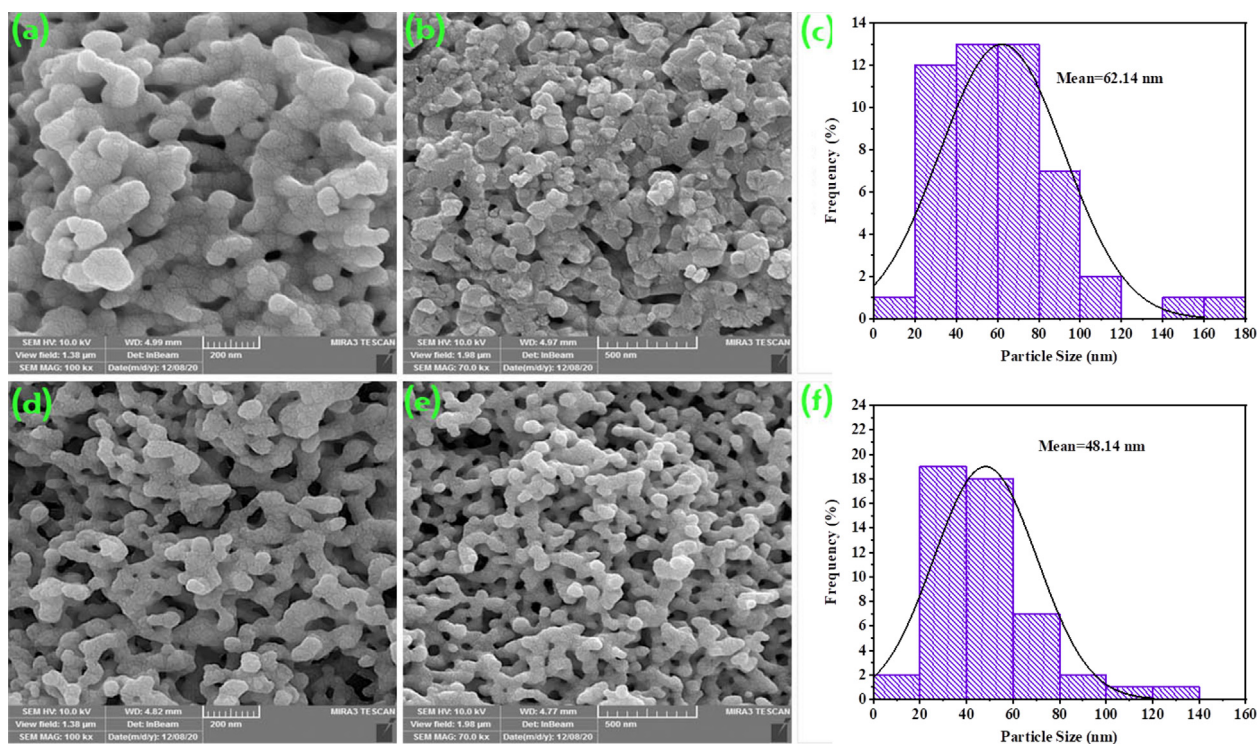


Fig. 6 The SEM images and corresponding particle size distribution of Tb-Co-O nanocomposites with various pH adjustment agents (a-c) sample no. 8 and (d-f) sample no.9.

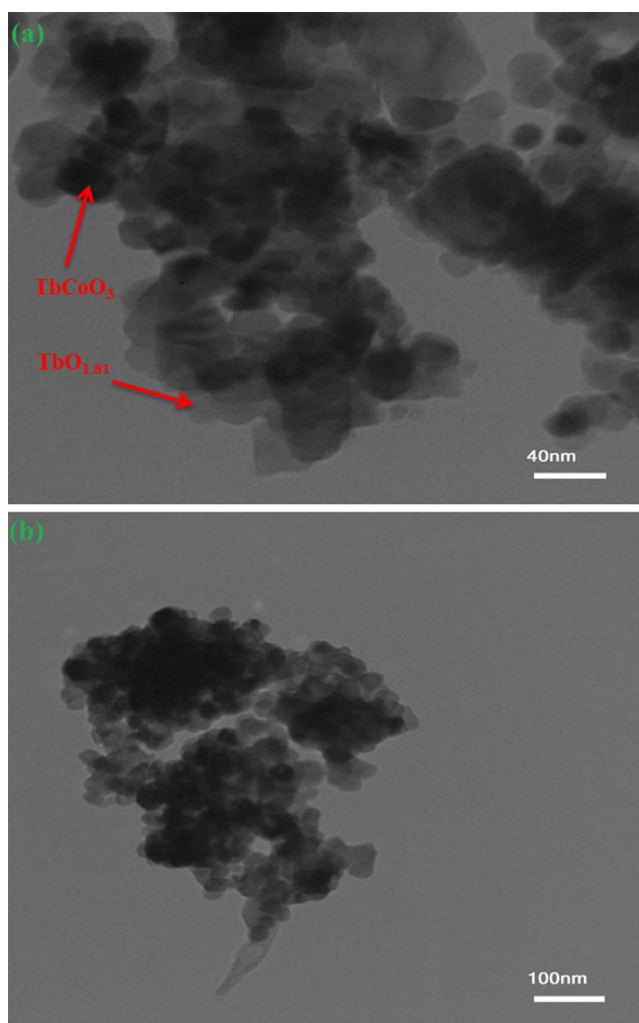


Fig. 7 TEM images of Tb-Co-O nanocomposites for different magnifications (sample no.6).

and 344 nm, which are related to the band gap (B.G.) energies of 2.95 and 3.20 eV, respectively, as estimated from the Tauc's equation: $(\alpha h\nu)^{1/n} = \beta(h\nu - \text{B.G.})$ (3); where α , $h\nu$, β , and B.G. means absorption coefficient, photon energy, a material constant parameter, and the energy of the optical bandgap, respectively. n is 2 or 1/2 for indirect and direct allowed transitions (Monsef et al., 2021b; Salavati-Niasari, 2005). It is worth noting that narrow band gap energy of the $\text{TbCoO}_3/\text{TbO}_{1.81}$ nanostructures may markedly provide by the defect level in oxygen-related positions of perovskite structures (Wu et al., 2017).

3.7. Photocatalytic performance

The dependency rate of the photocatalytic decolorization of $\text{TbCoO}_3\text{-TbO}_{1.81}$ nanocomposites synthesized in the presence of valerian (sample no. 6) was examined by diverse concentrations of AB 1 dye under UV light, as shown in Fig. 11. According to the results, it can be seen that a further increase in dye concentration up to 15 ppm lead to a reduced efficiency of photodegradation after 120 min of irradiation. With varying dye concentration from 10 to 15 ppm, the degradation percent-

age could be decreased from 63 % to 53 %. The main reason behind this fact is that by increasing AB 1 concentration, the photo-reaction probability between generated oxidizing agents and dye molecules will be induced in molecular level, which is related to the lowering of light penetrating power on the catalyst surface (Abdullah and Chong, 2010).

The photo-degradation efficacy of binary Tb-Co-O nanocomposites was recorded by employing three different toxic pollutants, namely EY, AV7, and AB1, and the changes in their light sources. Fig. 12 shows a comparison study of these organic colorants over the hetero-structured materials under UV light illumination. The UV-photoreaction of the Tb-Co-O semiconductors was conducted for 120 min. The decolorization percentages of EY molecules for sample nos.2 and 4-7 were calculated to be 66.0 %, 72.0 %, 84.0 %, 88.0 % and 80.0 %, respectively, as shown in Fig. 12a. From Fig. 12b, it can be seen that the photodegradation rates achieved using AV7 as organic pollutant were around 55.0 %, 60.0 %, 70.0 %, 72.0 %, and 75.0 % for sample nos.2 and 4-7, respectively. Also, the effects of the presence of AB1 molecules on the photocatalytic reaction of Tb-Co-O nanocomposites (sample nos.2 and 4-7 (Fig. 12c)) were found to be the decolorization percentages of 43.0 %, 46.0 %, 53.0 %, 63.0 %, and 59.0 %, respectively. Comparatively, the photo-catalytic compounds were also tested under visible light illumination. Fig. 13a shows an evaluation of the degradation ability of EY by the following decreasing trend: sample no. 4 (45.0 %) < sample no. 2 (50.0 %) < sample no. 5 (58.0 %) < sample no. 7 (66.0 %) < sample no. 6 (70.0 %). It can be observed that sample no. 6 has a higher photocatalytic output compared to other counterparts. However, the photocatalytic efficiencies of this product (sample no. 6) for AB1 (Fig. 13c) and AV7 (Fig. 13b) were calculated to be 48.0 %, and 58.0 % respectively. The blank experiments for degradation of EY, AV7 and AB1 were conducted under UV and visible lights without as-formed catalysts. According to the Figs. 12 and 13, the degradation percentages of EY, AV7 and AB1 were 20 %, 12 % and 14 % in the presence of UV light, while in the visible light were found to be 12 %, 11 % and 22 %, respectively. Based on the mentioned results, we believe that binary Tb-Co-O nanocomposites synthesized by coupled templates of valerian extract and en can act as a novel photosensitizer for water treatment operation. This sample with narrow particle distribution and higher surface area lead to the production of numerous active sites over the target material surface, which has a positive effect in enlarging active radicals and then higher photocatalytic activity. Table 2 summarizes the photodegradation efficiency of different perovskite compounds under visible and UV light. As demonstrated in this table, the $\text{TbCoO}_3/\text{TbO}_{1.81}$ nanocomposites can compete with other materials as a photocatalyst.

3.8. Mechanism of the photocatalytic reactions.

The ability of light-harvesting for nano-catalysts based on Tb-Co-O structures can be examined under the irradiation of visible and UV light sources. It is known that the produced electron - hole pairs of binary semiconductor play a vital role in the catalytic process, when light illumination is switch on ($h\nu \geq 2.95, 3.20$ eV). According to the inner electric structure, the photo-induced electrons (e^-) in the valence band (VB) can

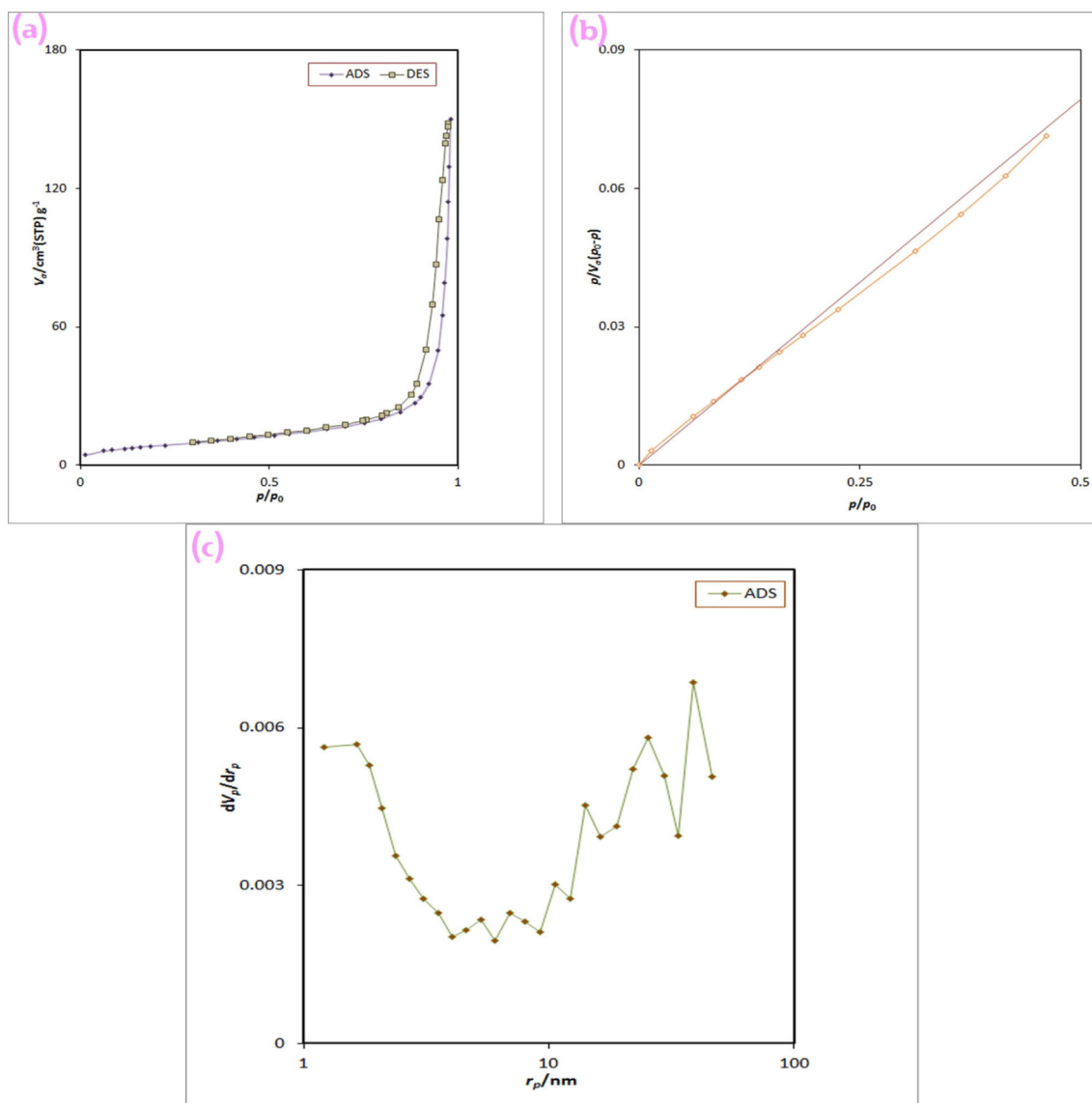


Fig. 8 (a) N_2 adsorption/desorption isotherm, (b) BET plot, and (c) BJH plot of Tb-Co-O nanocomposites (sample no.6).

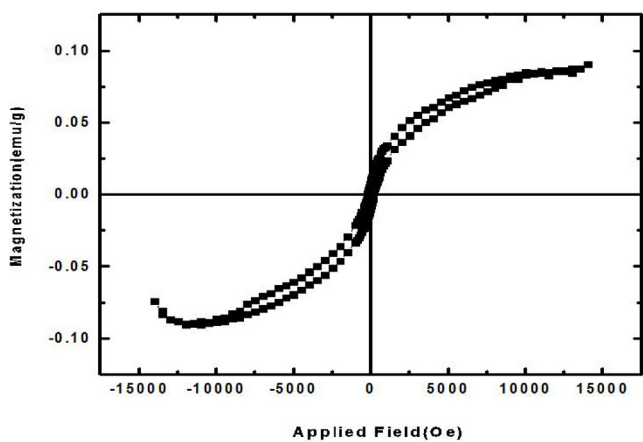


Fig. 9 Magnetization versus applied magnetic field at room temperature for sample no.6.

be excited slowly on the surface of conduction band (CB), making the aggregated holes (h^+) in VB. Specifically, the carrier transfer of e^- can be trapped easily by dissolved O_2 molecules on the surface of catalyst to produce $O_2\bullet^-$ radicals. On the other hand, the active holes provide a suitable background for direct reaction with the adsorbed hydroxyl or H_2O molecules to form the $OH\bullet$ radicals, leading to the oxidation of organic dyes during photodegradation process. These multiple active species such as $\bullet O_2^-$, $OH\bullet$, and h^+ radicals together with peroxide radicals can greatly affect the oxidation and /or reduction reactions during photocatalytic tests. The mechanistic insight of photocatalytic degradation for binary Tb-Co-O nanostructure was evaluated *via* employing the trapping experiments of active species including radicals of hydroxyl, holes and anions of superoxide. Here, the edetate disodium (EDTA-2Na), benzoic acid (BA), and 1,4-benzoquinone (BQ) were introduced into the reaction progress for scavenging h^+ , $OH\bullet$, and $\bullet O_2^-$, respectively. The potential effect of these radical components in percent of dye removal has been illus-

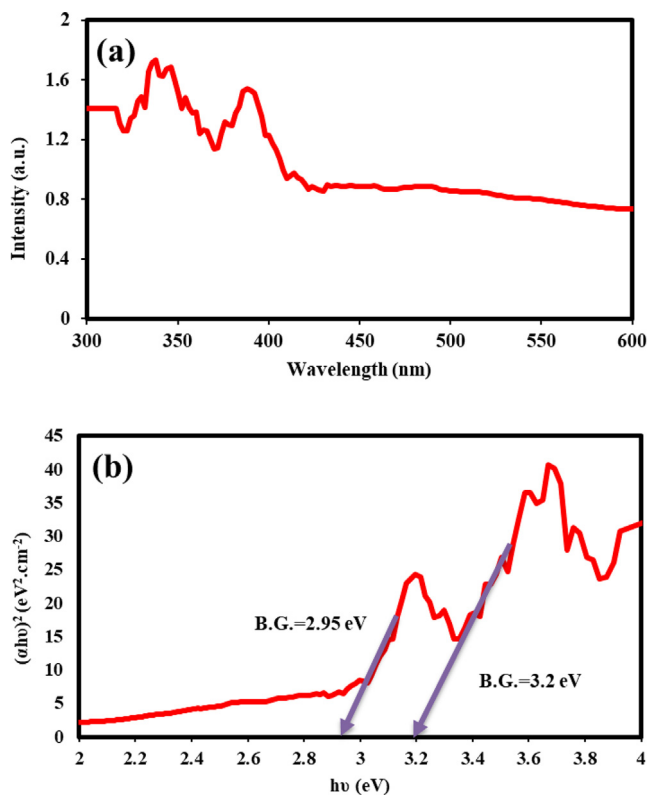


Fig. 10 (a) DRS spectrum, and (b) Optical density $(\alpha h\nu)^2$ versus $(h\nu)$ of Tb-Co-O nanocomposites (sample no.6).

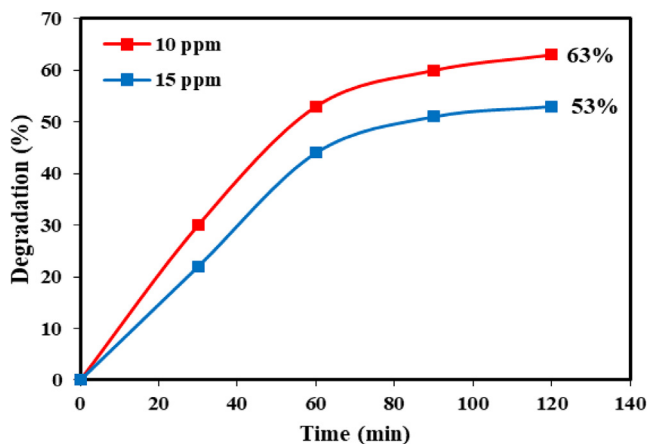


Fig. 11 Study the photocatalytic performance of Tb-Co-O nanocomposites (sample no.6) in diverse pollutant concentrations (AB1) under UV light.

trated in Fig. 14. It is clearly seen that the addition of EDTA-2Na play an important role in photocatalytic efficiency of EY with a significant reduction from 88.0 % to 49 %. However, in the presence of BA and BQ in the reaction solution, less than 8.0 % removal of EY was observed, suggesting that the $\text{OH}\bullet$, and $\text{O}_2^{\bullet-}$ were not responsible species in direction mechanism. Based on the previous research, the probable mechanism for the photocatalytic efficiency of organic dyes can be represented as follows (Guo et al., 2011):

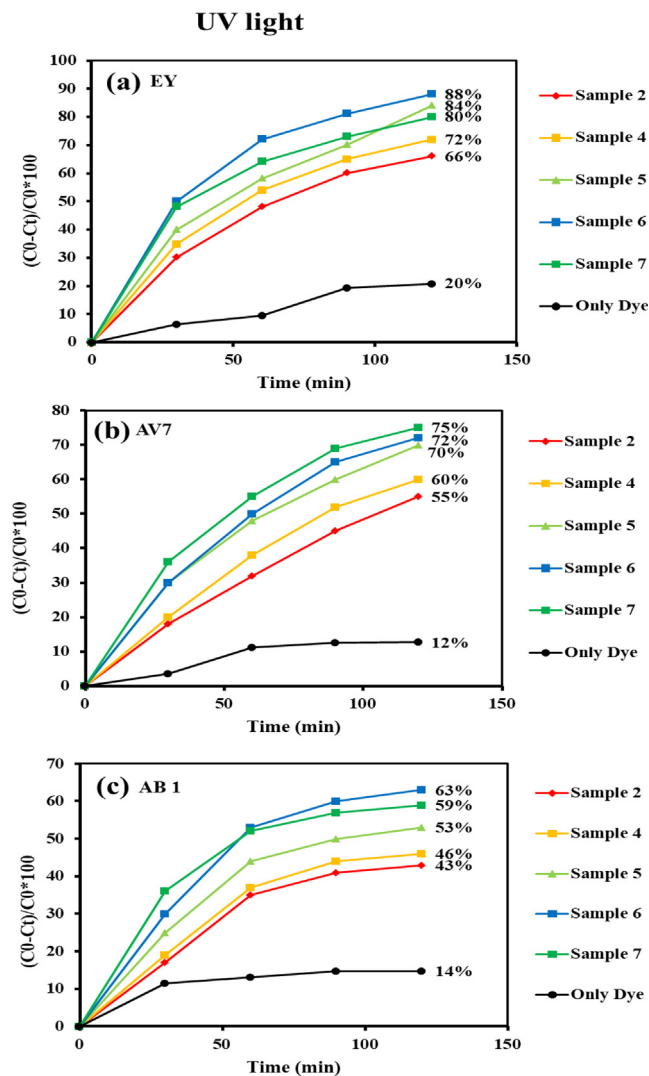
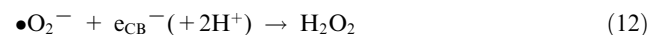
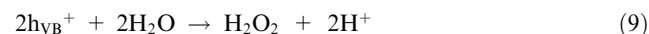
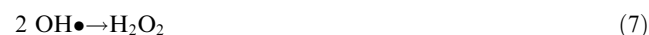
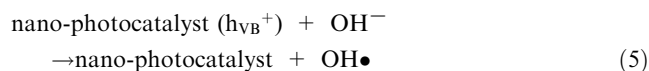
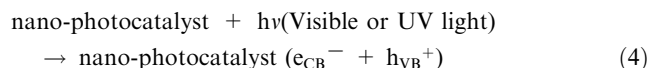


Fig. 12 Photocatalysis performance of Tb-Co-O nano-photocatalysts for removal of (a) EY, (b) AV7, and (c) AB 1 under UV light for 120 min.



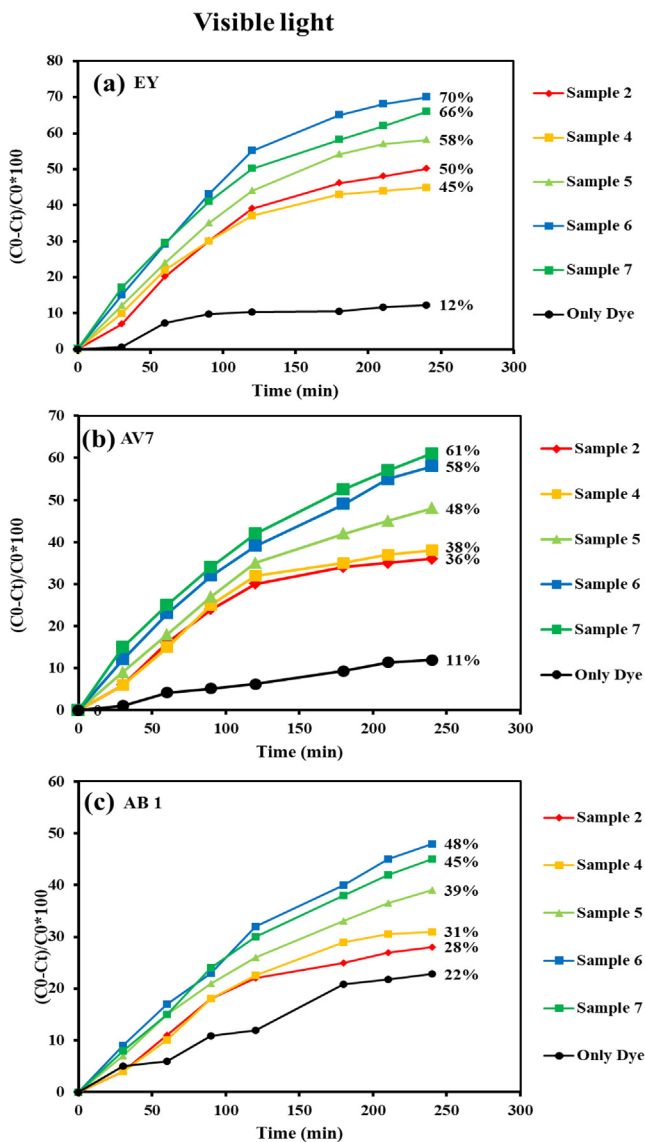


Fig. 13 Photocatalysis performance of Tb-Co-O nano-photocatalysts for removal of (a) EY, (b) AV 7, and (c) AB1 under visible light for 240 min.

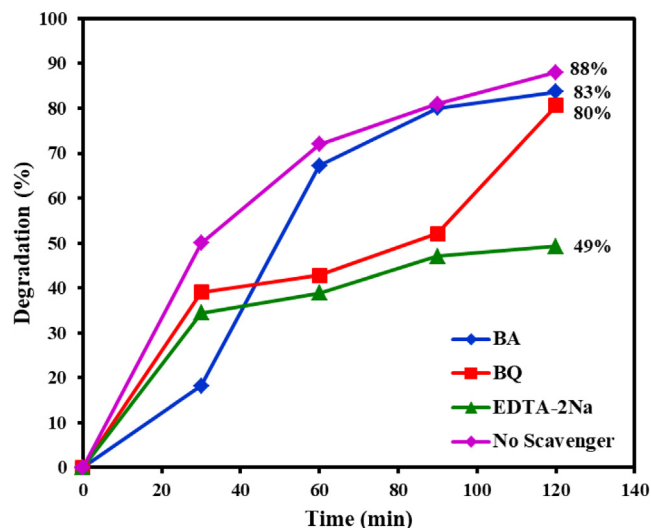


Fig. 14 Radical trapping experiment of active species including BQ, BA, and EDTA in the photocatalytic degradation of EY over the Tb-Co-O nano-photocatalysts.

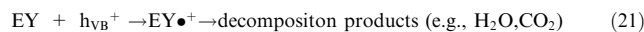
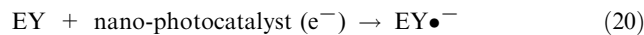
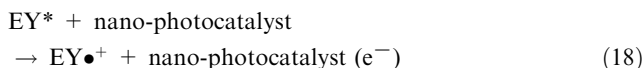
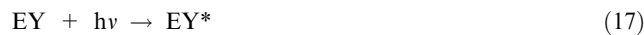


Table 2 Comparison of the photodegradation performances of our synthesized Tb-Co-O products with other materials reported in previous works.

Catalyst type	Fabrication method	Light source	Irradiation time (min)	Photodegradation efficiency (%)	Ref.
LaCoO ₃	Sol-gel method	150 W visible light lamp	150 min	63 % (MB ^a)	(Mocwana et al., 2022)
LaFeO ₃ nanocubes	Hydrothermal process	150 W high pressure mercury lamp	180 min	76.81 % (RhB ^b)	(Thirumalairajan et al., 2013)
LaCoO ₃	Metal citrate complex method	300 W Xe lamp	40 min	15.06 % (BPA ^c)	(Guo et al., 2017)
NaTaO ₃	Hydrothermal process	A 500 W Xe lamp	200 min	60 % (MB)	(Su et al., 2012)
La ₂ Ti ₂ O ₇	Polymeric complex	4 W UV lamps	90 min	55 % (MO ^d)	(Li et al., 2006)
LaNiO ₃	Sol-gel combustion method	400 W xenon lamp	5 h	74.9 % (MO)	(Li et al., 2010)
Tb-Co-O	Microwave method	400 W UV	120 min	88.0 % (EY)	This study

^a Methylene Blue.

^b Rhodamine B.

^c Bisphenol A.

^d Methyl Orange.

4. Conclusions

The present work demonstrates a fast microwave synthesis of novel monodisperse TbCoO₃/TbO_{1.81} nanocomposites *via* employing the valerian distillate as natural surfactants and en as alkaline agent. The impact of a variety of chemical and natural directing agents as well as base groups on particle size and shape of nanostructures was investigated. Also, to evaluate the textural, morphological, mesoporosity, and magnetic properties of nanoparticles, a series of physico-chemical analyses were employed. According to the results, the optimized nanostructures with the average grain size of 21.5 nm could be provided optical band-gaps of approximately 2.95 and 3.20 eV for nanocomposite, suggesting good photostability for degradation of organic pollutants such as EY, AV7, and ABI under visible and UV light treatments. This configuration of the Tb-Co-O nanophotocatalysts had a comparison study of photodegradation efficiency under UV and visible light illumination. The photocatalysis yield of TbCoO₃/TbO_{1.81} nanocomposites prepared by both natural template of valerian distillate and alkaline template of en (sample no. 6) was very much than those of other counterparts (with a high efficiency of 88 % for EY removal). Such studies confirmed that the geometric coordination for natural extract along with hydroxyl groups of amine template lead to a kinetic control over nucleation stage and growth mechanism of formed crystals. It is hoped that our current research may provide the potential of new nanocomposites based on Tb-Co-O nanostructures as an efficient semiconductor in environmental cleaning.

CRediT authorship contribution statement

Pourya Mehdizadeh: Software, Investigation, Methodology, Formal analysis. **Mina Jamdar:** Investigation, Methodology, Formal analysis. **Makarim A. Mahdi:** Writing – review & editing, Software, Visualization. **Waleed K. Abdulsahib:** Writing – review & editing, Software, Validation. **Layth S. Jasim:** Writing – review & editing, Software, Conceptualization. **Seyede Raheleh Yousefi:** Writing – original draft, Software. **Masoud Salavati-Niasari:** Formal analysis, Methodology, Writing – review & editing, Writing – original draft, Conceptualization, Supervision, Project administration, Investigation, Data curation, Validation, Resources, Visualization, Funding acquisition.

Declaration of Competing Interest

The authors declare that they have no known competing financial interests or personal relationships that could have appeared to influence the work reported in this paper.

Acknowledgements

Authors are grateful to the council of Iran National Science Foundation (INSF, 97017837) and University of Kashan, Grant No (159271/PM8) for supporting this work.

References

- Abdullah, M., Chong, F.K., 2010. Preparation and characterization of tungsten-loaded titanium dioxide photocatalyst for enhanced dye degradation. *J. Hazard. Mater.* 176, 451–458.
- Álvarez-Galván, M.C., Constantinou, D.A., Navarro, R.M., Villoria, J.A., Fierro, J.L.G., Efstathiou, A.M., 2011. Surface reactivity of LaCoO₃ and Ru/LaCoO₃ towards CO, CO₂ and C₃H₈: Effect of H₂ and O₂ pretreatments. *Appl. Catal. B: Environ.* 102, 291–301.
- Chiam, S.-L., Pung, S.-Y., Yeoh, F.-Y., 2020. Recent developments in MnO₂-based photocatalysts for organic dye removal: a review. *Environ. Sci. Pollut. Res.* 27, 5759–5778.
- Enrico, A., Costamagna, P., 2014. Model of infiltrated La_{1-x}Sr_xCo_{1-y}Fe_yO_{3-δ} cathodes for intermediate temperature solid oxide fuel cells. *J. Power Sources* 272, 1106–1121.
- Fujishima, A., Honda, K., 1972. Electrochemical photolysis of water at a semiconductor electrode. *nature* 238, 37–38.
- Gavrikov, A.V., Ilyukhin, A.B., Belova, E.V., Yapyrintsev, A.D., Dobrokhotova, Z.V., Khrushcheva, A.V., Efimov, N.N., 2020. Rapid preparation of SmCoO₃ perovskite via uncommon though efficient precursors: Composition matters! *Ceram. Int.* 46, 13014–13024.
- Gerbec, J.A., Magana, D., Washington, A., Strouse, G.F., 2005. Microwave-enhanced reaction rates for nanoparticle synthesis. *J. Am. Chem. Soc.* 127, 15791–15800.
- González-Casamachin, D.A., De la Rosa, J.R., Lucio-Ortiz, C.J., De Rio, D.A.D.H., Martínez-Vargas, D.X., Flores-Escamilla, G.A., Guzman, N.E.D., Ovando-Medina, V.M., Moctezuma-Velazquez, E., 2019. Visible-light photocatalytic degradation of acid violet 7 dye in a continuous annular reactor using ZnO/PPy photocatalyst: synthesis, characterization, mass transfer effect evaluation and kinetic analysis. *Chem. Eng. J.* 373, 325–337.
- Guo, J., Dai, Y.-Z., Chen, X.-J., Zhou, L.-L., Liu, T.-H., 2017. Synthesis and characterization of Ag₃PO₄/LaCoO₃ nanocomposite with superior mineralization potential for bisphenol A degradation under visible light. *J. Alloys Compd.* 696, 226–233.
- Guo, J., Li, P., Yang, Z., 2019. A novel Z-scheme g-C₃N₄/LaCoO₃ heterojunction with enhanced photocatalytic activity in degradation of tetracycline hydrochloride. *Catal. Commun.* 122, 63–67.
- Guo, M.Y., Ng, A.M.C., Liu, F., Djurišić, A.B., Chan, W.K., 2011. Photocatalytic activity of metal oxides—the role of holes and OH radicals. *Appl. Catal. B: Environ.* 107, 150–157.
- He, Y., Rao, H., Song, K., Li, J., Yu, Y., Lou, Y., Li, C., Han, Y., Shi, Z., Feng, S., 2019. 3D hierarchical ZnIn₂S₄ nanosheets with rich Zn vacancies boosting photocatalytic CO₂ reduction. *Adv. Funct. Mater.* 29, 1905153.
- Jiamprasertboon, A., Okamoto, Y., Hiroi, Z., Siritanon, T., 2014. Thermoelectric properties of Sr and Mg double-substituted LaCoO₃ at room temperature. *Ceram. Int.* 40, 12729–12735.
- Jung, W.Y., Hong, S.-S., 2013. Synthesis of LaCoO₃ nanoparticles by microwave process and their photocatalytic activity under visible light irradiation. *J. Ind. Eng. Chem.* 19, 157–160.
- Jusoh, N.W., Jalil, A.A., Triwahyono, S., Setiabudi, H.D., Sapawe, N., Satar, M.A., Karim, A.H., Kamarudin, N.H., Jusoh, R., Jaafar, N.F., 2013. Sequential desilication–isomorphous substitution route to prepare mesostructured silica nanoparticles loaded with ZnO and their photocatalytic activity. *Appl. Catal. A: Gen.* 468, 276–287.
- Kaur, A., Gupta, U., 2012. Simultaneous spectrophotometric determination of eosin and erythrosine in pharmaceutical and food samples by using mean centering of ratio spectra method. *Int. J. Res. Chem. Environ.* 2, 55–62.
- Lee, S.-Y., Park, S.-J., 2013. TiO₂ photocatalyst for water treatment applications. *J. Ind. Eng. Chem.* 19, 1761–1769.
- Leong, S., Razmjou, A., Wang, K., Hapgood, K., Zhang, X., Wang, H., 2014. TiO₂ based photocatalytic membranes: A review. *J. Membr. Sci.* 472, 167–184.
- Li, Z., Xue, H., Wang, X., Fu, X., 2006. Characterizations and photocatalytic activity of nanocrystalline La_{1-x}Ln_xTi₂O₇ (Ln = Pr, Gd, Er) solid solutions prepared via a polymeric complex method. *J. Mol. Catal. A Chem.* 260, 56–61.
- Li, Y., Yao, S., Wen, W., Xue, L., Yan, Y., 2010. Sol–gel combustion synthesis and visible-light-driven photocatalytic property of perovskite LaNiO₃. *J. Alloys Compd.* 491, 560–564.
- Malathi, A., Arunachalam, P., Madhavan, J., Al-Mayouf, A.M., Ghanem, M.A., 2018. Rod-on-flake α-FeOOH/BiOI nanocomposite: facile synthesis, characterization and enhanced photocatalytic

- performance. *Colloids Surf. A Physicochem. Eng. Asp.* 537, 435–445.
- Malathi, A., Madhavan, J., 2017. Synthesis and characterization of CuS/CdS photocatalyst with enhanced visible light-photocatalytic activity. *J. Nano Res. Trans Tech Publ.* 49–61.
- Megarajan, S.K., Rayalu, S., Nishibori, M., Labhsetwar, N., 2015. Improved catalytic activity of PrMO_3 ($M = \text{Co}$ and Fe) perovskites: synthesis of thermally stable nanoparticles by a novel hydrothermal method. *New J. Chem.* 39, 2342–2348.
- Meng, A., Zhang, L., Cheng, B., Yu, J., 2019. Dual cocatalysts in TiO_2 photocatalysis. *Adv. Mater.* 31, 1807660.
- Michel, C.R., Lopez-Alvarez, M.A., Martínez-Preciado, A.H., Carbal-Ariza, G.G., 2019. Novel UV sensing and photocatalytic properties of DyCoO_3 . *J. Sens.* 2019.
- Miranda-García, N., Maldonado, M.I., Coronado, J., Malato, S., 2010. Degradation study of 15 emerging contaminants at low concentration by immobilized TiO_2 in a pilot plant. *Catal. Today* 151, 107–113.
- Mittal, A., Mittal, J., Kurup, L., Singh, A., 2006. Process development for the removal and recovery of hazardous dye erythrosine from wastewater by waste materials—bottom ash and de-oiled soya as adsorbents. *J. Hazard. Mater.* 138, 95–105.
- Mochinaga, R., Arakawa, T., 2001. The gas-sensing of $\text{GdCoO}_3/\text{MO}_x$ ($M =$ transition metals) element having a heterojunction. *Sens. Actuators B Chem.* 77, 196–199.
- Mocwana, M.L., Mokoena, P.P., Mbule, P.S., Beas, I.N., Kabongo, G.L., Ogugua, S.N., Tshabalala, T.E., 2022. Photocatalytic Degradation of Methylene Blue and Ortho-Toluidine Blue: Activity of Lanthanum Composites La_xMO_y ($M: \text{Fe Co, Ni}$). *Catalysts* 12, 1313.
- Monsef, R., Ghiyasiyan-Arani, M., Salavati-Niasari, M., 2021a. Design of magnetically recyclable ternary $\text{Fe}_2\text{O}_3/\text{EuVO}_4/\text{g-C}_3\text{N}_4$ nanocomposites for photocatalytic and electrochemical hydrogen storage. *ACS Appl. Energy Mater.* 4, 680–695.
- Monsef, R., Soofivand, F., Alshamsi, H.A., Al-Nayili, A., Ghiyasiyan-Arani, M., Salavati-Niasari, M., 2021b. Sonochemical synthesis and characterization of PrVO_4/CdO nanocomposite and their application as photocatalysts for removal of organic dyes in water. *J. Mol. Liq.* 336, 116339.
- Moon, J.-W., Seo, W.-S., Okabe, H., Okawa, T., Koumoto, K., 2000. Ca-doped RCO_3 ($R = \text{Gd, Sm, Nd, Pr}$) as thermoelectric materials. *J. Mater. Chem.* 10, 2007–2009.
- Nur, A.S., Sultana, M., Mondal, A., Islam, S., Robel, F.N., Islam, M. A., Sumi, M.S.A., 2022. A review on the development of elemental and codoped TiO_2 photocatalysts for enhanced dye degradation under UV-vis irradiation. *J. Water Process. Eng.* 47, 102728.
- Ong, C.B., Ng, L.Y., Mohammad, A.W., 2018. A review of ZnO nanoparticles as solar photocatalysts: Synthesis, mechanisms and applications. *Renew. Sustain. Energy Rev.* 81, 536–551.
- Paprocki, A., Santos, H.S.d., Hammerschitt, M.E., Pires, M., Azevedo, C., 2010. Ozonation of azo dye acid black 1 under the suppression effect by chloride ion. *J. Braz. Chem. Soc.* 21, 452–460.
- Salavati-Niasari, M., 2005. Nanoscale microreactor-encapsulation of 18-membered decaaza macrocycle nickel (II) complexes. *Inorganic Chemistry Communications* 8 (2), 174–177. <https://doi.org/10.1016/j.inoche.2004.11.004>.
- Salavati-Niasari, M., 2006. Host (nanocavity of zeolite-Y)-guest (tetraaza[14]annulene copper(II) complexes) nanocomposite materials: Synthesis, characterization and liquid phase oxidation of benzyl alcohol. *Journal of Molecular Catalysis A: Chemical* 245 (1–2), 192–199. <https://doi.org/10.1016/j.molcata.2005.09.046>.
- Salavati-Niasari, M., Shakouri-Arani, M., Davar, F., 2008. Flexible ligand synthesis, characterization and catalytic oxidation of cyclohexane with host (nanocavity of zeolite-Y)/guest (Mn(II) , Co(II) , Ni(II) and Cu(II)) complexes of tetrahydro-salophen) nanocomposite materials. *Microporous and mesoporous materials* 116 (1–3), 77–85. <https://doi.org/10.1016/j.micromeso.2008.03.015>.
- Salavati-Niasari, M., Dadkhah, M., Davar, F., 2009. Synthesis and characterization of pure cubic zirconium oxide nanocrystals by decomposition of bis-aqua, tris-acetylacetonato zirconium (IV) nitrate as new precursor complex. *Inorganica Chimica Acta* 362 (11), 3969–3974. <https://doi.org/10.1016/j.ica.2009.05.036>.
- Saravanakumar, K., Muthuraj, V., Jeyaraj, M., 2018. The design of novel visible light driven Ag/CdO as smart nanocomposite for photodegradation of different dye contaminants. *Spectrochim. Acta A Mol. Biomol. Spectrosc.* 188, 291–300.
- Singhal, N., Selvaraj, S., Sivalingam, Y., Venugopal, G., 2022. Study of photocatalytic degradation efficiency of rGO/ZnO nano-photocatalyst and their performance analysis using scanning Kelvin probe. *J. Environ. Chem. Eng.* 10, 107293.
- Su, Y., Wang, S., Meng, Y., Han, H., Wang, X., 2012. Dual substitutions of single dopant Cr^{3+} in perovskite NaTaO_3 : synthesis, structure, and photocatalytic performance. *RSC Adv.* 2, 12932–12939.
- Teng, Z., Yang, N., Lv, H., Wang, S., Hu, M., Wang, C., Wang, D., Wang, G., 2019. Edge-functionalized $\text{g-C}_3\text{N}_4$ nanosheets as a highly efficient metal-free photocatalyst for safe drinking water. *Chem* 5, 664–680.
- Thirumalairajan, S., Girija, K., Hebalkar, N.Y., Mangalaraj, D., Viswanathan, C., Ponpandian, N., 2013. Shape evolution of perovskite LaFeO_3 nanostructures: a systematic investigation of growth mechanism, properties and morphology dependent photocatalytic activities. *RSC Adv.* 3, 7549–7561.
- Tugova, E.A., Karpov, O.N., 2021. Glycine-nitrate combustion engineering of neodymium cobaltite nanocrystals. *Rare Met.* 40, 1778–1784.
- Upadhyay, R.K., Soin, N., Roy, S.S., 2014. Role of graphene/metal oxide composites as photocatalysts, adsorbents and disinfectants in water treatment: a review. *RSC Adv.* 4, 3823–3851.
- Wang, H., Li, G., Li, L., 2016. Influence of Mn-substitution on the structure and low-temperature electrical conduction properties of PrCoO_3 . *Ceram. Int.* 42, 12283–12288.
- Wang, L., Pang, Q., Song, Q., Pan, X., Jia, L., 2015. Novel microbial synthesis of Cu doped LaCoO_3 photocatalyst and its high efficient hydrogen production from formaldehyde solution under visible light irradiation. *Fuel* 140, 267–274.
- Wang, S., Wang, Y., Zhang, S.L., Zang, S.Q., Lou, X.W., 2019. Supporting ultrathin ZnIn_2S_4 nanosheets on Co/N-Doped graphitic carbon nanocages for efficient photocatalytic H_2 generation. *Adv. Mater.* 31, 1903404.
- Wang, J.L., Xu, L.J., 2012. Advanced oxidation processes for wastewater treatment: formation of hydroxyl radical and application. *Crit. Rev. Environ. Sci. Technol.* 42, 251–325.
- Wang, R., Ye, C., Wang, H., Jiang, F., 2020. Z-scheme $\text{LaCoO}_3/\text{g-C}_3\text{N}_4$ for efficient full-spectrum light-simulated solar photocatalytic hydrogen generation. *ACS omega* 5, 30373–30382.
- Wen, J., Xie, J., Chen, X., Li, X., 2017. A review on $\text{g-C}_3\text{N}_4$ -based photocatalysts. *Appl. Surf. Sci.* 391, 72–123.
- Wu, M., Luo, M., Guo, M., Jia, L., 2017. Sugarcane bagasse hydrolysis by metal ions mediated synthesis of perovskite LaCoO_3 and the photocatalytic performance for hydrogen from formaldehyde solution under visible light. *ACS Sustain. Chem. Eng.* 5, 11558–11565.
- Wu, W., Zhang, J., Cao, P., Dong, J., Ding, H., 2018. Synthesis of Sm-Co nanoparticles by sol-gel method. *Mod. Phys. Lett. B.* 32, 1840069.
- Xia, P., Cao, S., Zhu, B., Liu, M., Shi, M., Yu, J., Zhang, Y., 2020. Designing a 0D/2D S-scheme heterojunction over polymeric carbon nitride for visible-light photocatalytic inactivation of bacteria. *Angew. Chem. Int. Ed.* 59, 5218–5225.
- Xu, F., Meng, K., Cheng, B., Yu, J., Ho, W., 2019. Enhanced Photocatalytic Activity and Selectivity for CO_2 Reduction over a TiO_2 Nanofibre Mat Using Ag and MgO as Bi-Cocatalyst. *ChemCatChem* 11, 465–472.

- Yahya, N., Aziz, F., Jamaludin, N., Mutalib, M., Ismail, A., Salleh, W., Jaafar, J., Yusof, N., Ludin, N., 2018. A review of integrated photocatalyst adsorbents for wastewater treatment. *J. Environ. Chem. Eng.* 6, 7411–7425.
- Zhang, G., Gao, Y., Zhang, Y., Guo, Y., 2010. Fe₂O₃-pillared rectorite as an efficient and stable Fenton-like heterogeneous catalyst for photodegradation of organic contaminants. *Environ. Sci. Technol.* 44, 6384–6389.
- Zhang, W., Wang, M., Zhao, W., Wang, B., 2013. Magnetic composite photocatalyst ZnFe₂O₄/BiVO₄: synthesis, characterization, and visible-light photocatalytic activity. *Dalton Trans.* 42, 15464–15474.

Further reading

- Yeganeh-Faal, A., Bordbar, M., Negahdar, N., Nasrollahzadeh, M., 2017. Green synthesis of the Ag/ZnO nanocomposite using *Valeriana officinalis* L. root extract: application as a reusable catalyst for the reduction of organic dyes in a very short time. *IET Nanobiotechnol.* 11, 669–676.